



**HAL**  
open science

## Deep Convolutional Matching

Jerome Revaud, Philippe Weinzaepfel, Zaid Harchaoui, Cordelia Schmid

► **To cite this version:**

Jerome Revaud, Philippe Weinzaepfel, Zaid Harchaoui, Cordelia Schmid. Deep Convolutional Matching. 2015. hal-01148432v1

**HAL Id: hal-01148432**

**<https://inria.hal.science/hal-01148432v1>**

Preprint submitted on 4 Jun 2015 (v1), last revised 31 May 2016 (v3)

**HAL** is a multi-disciplinary open access archive for the deposit and dissemination of scientific research documents, whether they are published or not. The documents may come from teaching and research institutions in France or abroad, or from public or private research centers.

L'archive ouverte pluridisciplinaire **HAL**, est destinée au dépôt et à la diffusion de documents scientifiques de niveau recherche, publiés ou non, émanant des établissements d'enseignement et de recherche français ou étrangers, des laboratoires publics ou privés.

# Deep Convolutional Matching

Jerome Revaud  
Cordelia Schmid  
INRIA

firstname.lastname@inria.fr

Philippe Weinzaepfel

Zaid Harchaoui

the date of receipt and acceptance should be inserted later

**Abstract** We propose a new matching algorithm, called DeepMatching, to compute dense correspondences between images. DeepMatching relies on a deep, multi-layer, convolutional architecture designed for matching images. The proposed matching algorithm can handle non-rigid deformations and repetitive textures, and can therefore efficiently determine dense correspondences in the presence of significant changes between images.

We evaluate the performance of DeepMatching, in comparison with state-of-the-art matching algorithms, on resp. the Mikolajczyk (Mikolajczyk et al 2005), the MPI-Sintel (Butler et al 2012) and the Kitti (Geiger et al 2013) datasets. The performance measure is “Accuracy@ $T$ ”, that is the percentage of correct pixels for a specified error threshold of  $T$  pixels. DeepMatching outperforms the state-of-the-art algorithms in terms of accuracy@ $T$  and shows excellent results in particular for repetitive textures.

We also propose a method for estimating optical flow, called DeepFlow, by integrating a DeepMatching term in a variational energy minimization approach. Robustness to large displacements is obtained due to this matching term. DeepFlow obtains competitive performance on public benchmarks for optical flow estimation. In particular, DeepFlow obtains state-of-the-art results on the MPI-Sintel dataset (Butler et al 2012).

**Keywords** Non-rigid matching, optical flow, deep convolutional neural networks (CNN).

## 1 Introduction

Computing correspondences between related images is a central issue in many computer vision problems, ranging from scene recognition to optical flow estimation (Forsyth and Ponce 2011; Szeliski 2010). To sum it up, the goal of a matching algorithm is to discover shared visual content (in a broad sense, *e.g.* it could correspond to real objects or not) between two images, and to establish as many precise point-wise correspondences, called *matches*, as possible between the concerned regions. An essential aspect of matching approaches is the amount of rigidity they assume when computing the correspondences. In fact, matching approaches range between two extreme cases: stereo matching, where matching hinges upon strong geometric constraints, and matching “in the wild”, where the set of possible transforms from the source image to the target one is large and the problem is basically almost unconstrained. Effective approaches have been designed for matching rigid objects across images in the presence of large view-point changes (Lowe 2004; Barnes et al 2010; HaCohen et al 2011). However, the performance of current state-of-the-art matching algorithms for images “in the wild”, such as consecutive images in real-world videos featuring fast non-rigid motion, still calls for improvement (Xu et al 2012; Chen et al 2013). In this paper, we aim at tackling matching in such a general setting.

Matching algorithms for images in the wild need to accommodate several requirements, that turn out to be often in contradiction. On one hand, matching objects necessarily requires rigidity assumptions, to some extent. It is also mandatory that these objects own sufficiently discriminative textures to make the problem well-defined. On the other hand, many objects or regions do not behave as rigid objects, like humans or

animals. Furthermore, large portions of an image are usually occupied by weakly-to-no textured regions, often with repetitive textures, like sky or bucolic background.

Descriptor matching approaches, such as SIFT (Lowe 2004) or HOG (Dalal and Triggs 2005; Brox and Malik 2011) matching, compute discriminative feature representations from rectangular patches. However, while these approaches succeed in case of rigid motion, they fail to match regions with weak or repetitive textures, as local patches become poorly discriminative in these situations. Due to relying on large and rigid patches, they also usually yield very poor and imprecise matches in case of non-rigid deformations. Discriminative power can be traded against increased robustness to non-rigid deformations. Indeed, propagation-based approaches, such as Generalized PatchMatch (Barnes et al 2010) or Non-rigid Dense Correspondences (HaCohen et al 2011), compute simple feature representations from small patches and propagate the matching to neighboring patches. They yield good performance in case of non-rigid deformations. However, matching repetitive textures remains beyond the reach of these approaches.

We propose here a novel approach, called DeepMatching, that gracefully combines the strengths of these two families of approaches. DeepMatching benefits from three main properties. Matching is computed using a multi-layer architecture, which breaks down patches into a hierarchy of sub-patches. This architecture allows to essentially work at several scales and handle repetitive textures. Furthermore, within each layer, local matches are computed assuming a restricted set of feasible rigid deformations. Local matches are then propagated up the hierarchy using successive rectifications steps, which progressively discard spurious incorrect matches.

We make three contributions:

- **Dense correspondence matching:** we propose a matching algorithm, called DeepMatching, that allows to robustly determine dense correspondences between two input images. It explicitly handles non-rigid deformations, with bounds on the deformation tolerance, and incorporates a multi-scale scoring of the matches, making it robust to repetitive or weak textures.

- **Fast, scale/rotation-invariant matching:** we propose a computationally efficient version of DeepMatching, which performs almost as well as exact DeepMatching at a much lower memory cost. Furthermore, this fast version of DeepMatching is also amenable to a scale and rotation-invariant extension, making it an excellent competitor to state-of-the-art descriptor matching approaches.

- **Large-displacement optical flow:** we propose an optical flow approach based on DeepMatching and

variational energy minimization, called DeepFlow. Our approach is robust to large displacements and obtains state-of-the-art results on the MPI-Sintel dataset (Butler et al 2012).

This paper is organized as follows. After a review of previous works (Section 2), we start by presenting the proposed matching algorithm, DeepMatching, in Section 3. Then, Section 4 describes several extensions of DeepMatching. In particular, we propose an optical flow estimation approach termed DeepFlow in Section 4.3. Finally, we present experimental results in Section 5.

A preliminary version of this article has appeared in Weinzaepfel et al (2013). This version adds (1) an in-depth presentation of DeepMatching; (2) an enhanced version of DeepMatching, which improves the match scoring and the selection of entry points for backtracking; (3) proofs on time and memory complexity of DeepMatching as well as its deformation tolerance; (4) a discussion on the connection between Deep Convolutional Neural Networks and DeepMatching; (5) a fast approximate version of DeepMatching; (6) a scale and rotation invariant version of DeepMatching; and (7) an extensive experimental evaluation of DeepMatching on several state-of-the-art benchmarks.

## 2 Related work

We give a brief overview over related work in “general” image matching, that is matching with little prior knowledge and constraints, and matching for optical flow estimation, that is matching consecutive images in videos.

### 2.1 General image matching

Image matching based on local features has been extensively studied in the past decade. It has been applied successfully to various domains, such as wide baseline stereo matching (Furukawa et al 2010) and image retrieval (Philbin et al 2010). It consists of two steps: extraction of local descriptors and matching them. Image descriptors are extracted in rigid (generally square) local frames at sparse invariant image locations (Mikolajczyk et al 2005; Szeliski 2010). Matching then equals nearest neighbor matching between descriptors, followed by an optional geometric verification. While this class of technique is well suited to the case of well-textured rigid objects, it fails to match non-rigid objects or weakly textured regions.

In contrast, the proposed matching algorithm, called *DeepMatching*, is inspired by non-rigid 2D warping and deep convolutional networks (LeCun et al 1998a; Uchida

and Sakoe 1998; Keysers et al 2007). This family of approaches explicitly models non-rigid deformations. We employ a novel family of feasible warpings that does not enforce monotonicity nor continuity constraints, in contrast to traditional 2D warping (Uchida and Sakoe 1998; Keysers et al 2007). This makes the problem computationally much less expensive.

It is also worthwhile to mention the similarity with non-rigid matching approaches developed for a broad range of applications. Ecker and Ullman (2009) proposed a similar pipeline to ours (albeit more complex) to measure the similarity of small images. However, their method lacks a way of merging correspondences belonging to objects with contradictory motions, *e.g.*, on different focal planes. For the purpose of establishing dense correspondences between images, Wills et al (2006) estimated a non-rigid matching by robustly fitting smooth parametric models (homography and splines) to local descriptor matches. In contrast, our approach is non-parametric and model-free.

Recently, fast algorithms for dense patch matching have taken advantage of the redundancy between overlapping patches (Barnes et al 2010; Korman and Avidan 2011; Sun 2012). The insight is to propagate good matches to their neighborhood in a loose fashion, yielding dense non-rigid matching. In practice, however, the matching smoothness is unconstrained, leading to highly discontinuous match fields. HaCohen et al (2011) reinforce neighboring matches using an iterative multi-scale expansion and contraction strategy. Yet, the algorithm matches poorly discriminative patches and, as such, cannot overcome the inherent weaknesses of patch matching approaches. More recently, Kim et al (2013) proposed a hierarchical matching to obtain dense correspondences, using a coarse-to-fine (top-down) strategy. Loopy belief propagation is used to perform inexact inference.

In contrast to these approaches, DeepMatching proceeds bottom-up and, then, top-down. Due to the rectification steps interleaved between layers, DeepMatching handles poorly discriminative patches, and progressively discards incorrect spurious matches. The multi-layer construction allows to efficiently perform matching assuming semi-rigid local deformations. In addition, DeepMatching can be computed efficiently, and can be further accelerated to satisfy low-memory requirements with negligible loss in accuracy.

## 2.2 Matching for Optical Flow Estimation

Variational energy minimization is currently the most popular framework for optical flow estimation. Since

the pioneering work of Horn and Schunck (1981), research has focused on alleviating the drawbacks of this approach. A series of improvements were proposed over the years (Black and Anandan 1996; Werlberger et al 2009; Bruhn et al 2005; Papenberg et al 2006; Baker et al 2011; Sun et al 2014b; Vogel et al 2013a). The variational approach of Brox et al (2004) combines most of these improvements in a unified framework. The energy decomposes into several terms, resp. the data-fitting and the smoothness terms. Energy minimization is then performed by solving the Euler-Lagrange equations, reducing the problem to solving a sequence of large and structured linear systems.

More recently, the addition of a descriptor matching term in the energy to be minimized was proposed by Brox and Malik (2011). Following this idea, several papers (Tola et al 2008; Brox and Malik 2011; Liu et al 2011) show that dense descriptor matching improves performance. While it clearly helps to estimate large displacements, descriptor matching is unable to cope with non-rigid deformations and weak or repetitive textures. In fact, strategies to prune false matches such as reciprocal nearest-neighbor verification (Brox and Malik 2011), also eliminate as a side effects correct matches in weakly textured regions. Therefore, a variational energy minimization approach that includes such a descriptor matching term may fail at locations where matches are misleading or missing.

In the context of dense scene correspondence, descriptors or small patches were used in SIFT flow (Liu et al 2011) and PatchMatch (Barnes et al 2010) algorithms. Xu et al (2012) integrate matching of SIFT (Lowe 2004) and PatchMatch (Barnes et al 2010) to refine the flow initialization at each level. Excellent results were obtained for optical flow estimation, yet at the cost of expensive fusion steps. Leordeanu et al (2013) propose to extend sparse matching, with locally affine constraint, to dense matching before using a total variation algorithm to refine the flow estimation. We present here a computationally efficient and competitive approach for large displacement optical flow using the output of the proposed DeepMatching algorithm.

## 3 DeepMatching

This section introduces our matching algorithm DeepMatching. DeepMatching is effectively a correlation (convolutional) matching algorithm at patch-level, that proceeds in a multi-layer fashion. The correlation matching component performs matching of patches in the source image with patches in the target image. The multi-layer architecture is determined by a quadtree-like patch subdivision scheme, with an extra degree of freedom to

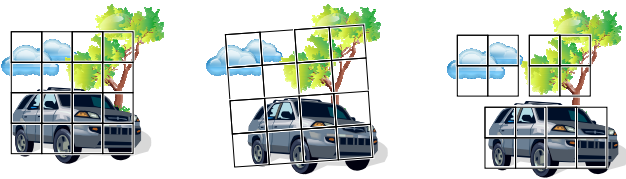


**Fig. 1** Illustration of moving quadrant similarity: a quadrant is a quarter of a SIFT patch, *i.e.* a group of  $2 \times 2$  cells. *Left*: SIFT descriptor in the first image. *Middle*: second image with optimal standard SIFT matching (rigid). *Right*: second image with optimal *moving quadrant* SIFT matching. In this example, the patch covers various objects moving in different directions: for instance the car moves to the right while the cloud to the left. Rigid matching fails to capture this whereas the moving quadrant approach is able to follow each object.

locally re-optimize the positions of each quadrant. In order to enhance the contrast of the spatial correlation maps output by the local correlation/convolution matches, a rectifying stage consisting in applying a non-linear transformation is interleaved in-between each layer.

We first give an overview of DeepMatching in Section 3.1 and show that it can be decomposed in a bottom-up pass followed by a top-down pass. We, then, present the bottom-up pass in Section 3.2 and the top-down on in Section 3.3. Finally, we discuss and highlight in Section 3.4 the specificities of DeepMatching compared to other matching approaches.

### 3.1 Overview of the approach

A standard approach for matching regions between two images is based on the SIFT descriptor (Lowe 2004). SIFT is a histogram of gradient orientations with  $4 \times 4$  spatial cells, yielding a robust descriptor  $\mathbf{R} \in \mathbb{R}^{128}$  that effectively encodes any square image region. Note that its  $4 \times 4$  cell grid can also be seen as 4 so-called ‘quadrants’ of  $2 \times 2$  cells, see Figure 1. We, then, rewrite it as  $\mathbf{R} = [\mathbf{R}_1, \mathbf{R}_2, \mathbf{R}_3, \mathbf{R}_4]$ , with  $\mathbf{R}_s \in \mathbb{R}^{32}$ .

Let  $\mathbf{R}$  and  $\mathbf{R}'$  be the SIFT descriptors of the corresponding regions in the source and target images. In order to cancel the effect of non-rigid motion, we propose to optimize the *positions*  $p_s \in \mathbb{R}^2$  of the 4 quadrants of the target descriptor  $\mathbf{R}'$  (rather than keeping them fixed), in order to maximize

$$\text{sim}(\mathbf{R}, \mathbf{R}') = \max_{\{p_s\}} \frac{1}{4} \sum_{s=1}^4 \text{sim}(\mathbf{R}_s, \mathbf{R}'_s(p_s)), \quad (1)$$

where  $\mathbf{R}'_s(p_s) \in \mathbb{C}^{32}$  is the descriptor of a single quadrant extracted at position  $p_s$  and  $\text{sim}(\cdot)$  a similarity function. Now,  $\text{sim}(\mathbf{R}, \mathbf{R}')$  is able to handle situations like in Figure 1 where a region contains multiple objects moving in different directions. Furthermore, if the four

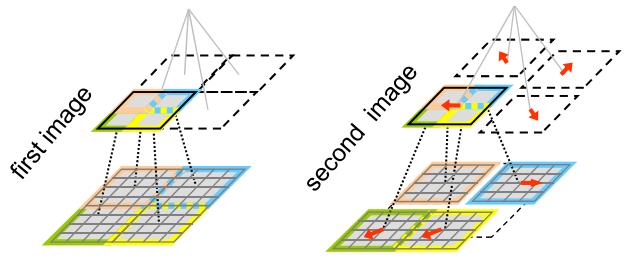


**Fig. 2** *Left*: Quadtree-like patch hierarchy in the first image. *Right*: one possible displacement of corresponding patches in the second image.

quadrants can move independently (of course, within some extent), it can be calculated more efficiently as:

$$\text{sim}(\mathbf{R}, \mathbf{R}') = \frac{1}{4} \sum_{s=1}^4 \max_{p_s} \text{sim}(\mathbf{R}_s, \mathbf{R}'_s(p_s)), \quad (2)$$

When applied recursively to each quadrant, this strategy allows for fine non-rigid matching. In other words, each quadrant is again subdivided into 4 sub-quadrants, and so on until a minimum patch size is reached. We shall refer to this minimum patch size as *atomic*. This recursive decomposition can be represented as a quadtree, see Figure 2. Given an initial pair of two matching regions, retrieving atomic patch correspondences is then done in a top-down fashion (*i.e.* by recursively applying eq. (2) on the quadrant’s positions  $\{p_s\}$ ).

Nevertheless, in order to first determine the set of matching regions between the two images, we need to compute beforehand the matching scores (*i.e.* similarity) of all large-enough patches in the two images (as in Figure 1), and keep the pairs with maximum similarity. As indicated by equation (2), the score is formed by averaging the max-pooled scores of the patch’s quadrants. Hence, the process of computing the matching scores is bottom-up. In the following, we call *correlation map* the matching scores of a single patch from the first image at every position in the second image. Selecting matching patches then corresponds to finding local maxima in the correlation maps.

To sum-up, the algorithm can be decomposed in two steps: (i) first, correlation maps are computed using a bottom-up algorithm, as shown in Figure 6. Correlation maps of small patches are first computed and then aggregated to form correlation maps of larger patches; (ii) next, a top-down method estimates the motion of atomic patches starting from matching pairs of large patches.

In the remainder of this section, we detail the two steps described above (Section 3.2 and Section 3.3), before analyzing the properties of DeepMatching in Section 3.4.

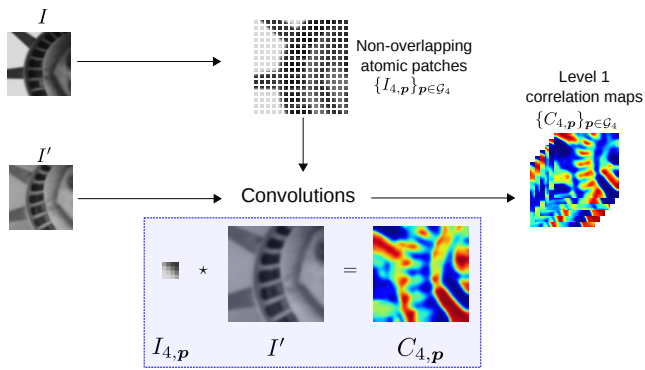


**Fig. 3** Computing the first level correlation maps  $\{C_{4,p}\}_{p \in \mathcal{G}_4}$ . Given two images  $I$  and  $I'$ , the first one is split into non-overlapping atomic patches of size  $4 \times 4$  pixels. For each patch, we compute the convolution with  $I'$  to obtain one correlation map per atomic patch (*bottom*).

### 3.2 Bottom-up correlation pyramid computation

Let  $I$  and  $I'$  be two images of resolution  $W \times H$  and  $W' \times H'$ .

*First level.* We use patches of size  $4 \times 4$  pixels as atomic patches. We split  $I$  into non-overlapping atomic patches, and compute the correlation map for each of them at every position in  $I'$ , see Figure 3. The score between two atomic patches  $\mathbf{R}$  and  $\mathbf{R}'$  is defined as the average of pixel-wise similarities:

$$\text{sim}(\mathbf{R}, \mathbf{R}') = \frac{1}{16} \sum_{i=1}^4 \sum_{j=1}^4 \mathbf{R}_{i,j}^\top \mathbf{R}'_{i,j}, \quad (3)$$

where each pixel  $\mathbf{R}_{i,j}$  is represented as a histogram of oriented gradients pooled over a local neighborhood. Note that since the pixel histograms are  $\ell_2$ -normalized, the similarity function takes value in  $[0, 1]$ .

We can express the correlation map computation more formally in a convolutional framework. Let  $I_{N,p}$  be a patch of size  $N \times N$  from the first image centered at  $\mathbf{p}$  ( $N \geq 4$  is a power of 2). Let  $\mathcal{G}_4 = \{2, 6, 10, \dots, W-2\} \times \{2, 6, 10, \dots, H-2\}$  be a grid of step 4 pixels.  $\mathcal{G}_4$  is the set of the centers of the atomic patches. For each  $\mathbf{p} \in \mathcal{G}_4$ , we convolve the patch  $I_{4,p}$  over  $I'$

$$C_{4,p} = I_{4,p} \star I', \quad (4)$$

to get the correlation map  $C_{4,p}$ . For any pixel  $\mathbf{p}'$  of  $I'$ ,  $C_{4,p}(\mathbf{p}')$  is a measure of similarity between  $I_{4,p}$  and  $I'_{4,p'}$ . Examples of such correlation maps are shown in Figure 3 and Figure 4. Without surprise we can observe that atomic patches are not discriminative. Recursive aggregation of patches in subsequent stages will be the key to create discriminative responses.

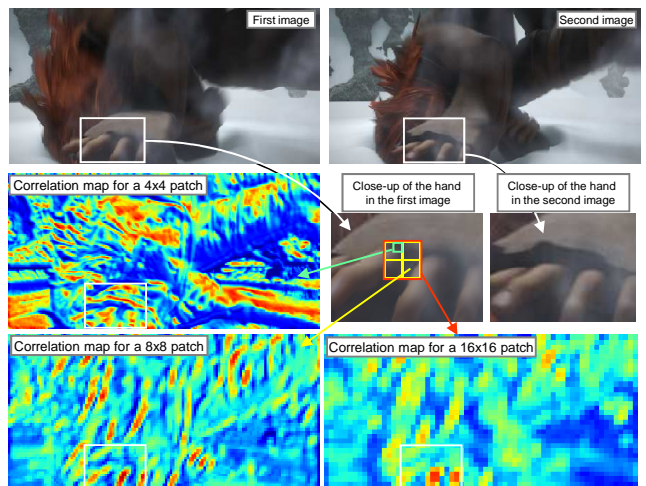


**Fig. 4** Correlation maps for patches of different size. *Middle-left:* correlation map of a  $4 \times 4$  patch. *Bottom-right:* correlation map of a  $16 \times 16$  patch obtained by aggregating correlation responses of children  $8 \times 8$  patches (*bottom-left*), themselves obtained from  $4 \times 4$  patches. The map of the  $16 \times 16$  patch is clearly more discriminative than previous ones despite the change in appearance of the region.

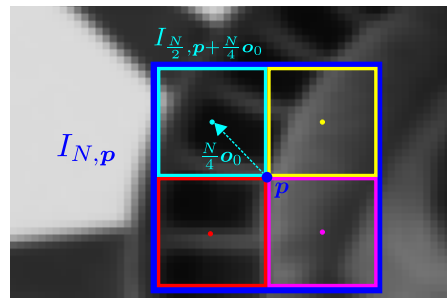


**Fig. 5** An image patch  $I_{N,p}$  (blue box) is composed of 4 quadrants  $I_{\frac{N}{2}, \mathbf{p} + \frac{N}{4} \mathbf{o}_i}$ ,  $i = 0 \dots 3$ .

*Iteration.* We then compute the correlation maps of larger patches formed by aggregating smaller patches. As shown in Figure 5, a  $N \times N$  patch  $I_{N,p}$  is the concatenation of 4 patches of size  $N/2 \times N/2$ :

$$I_{N,p} = \left[ I_{\frac{N}{2}, \mathbf{p} + \frac{N}{4} \mathbf{o}_i} \right]_{i=0..3} \quad \text{with} \quad \begin{cases} \mathbf{o}_0 = [-1, -1]^\top, \\ \mathbf{o}_1 = [-1, +1]^\top, \\ \mathbf{o}_2 = [+1, -1]^\top, \\ \mathbf{o}_3 = [+1, +1]^\top. \end{cases} \quad (5)$$

They correspond respectively to the top-left, bottom-left, top-right and bottom-right quadrants. The correlation map of  $I_{N,p}$  can thus be computed using its children's correlation maps. In the case of rigid matching, it would just amount to average them. For DeepMatching, we want to optimize the positions of the quadrants in a local neighborhood. This is achieved via a local max-pooling step: for each quadrant, we retain its maximum score over a small neighborhood.

In more details, at iteration  $\ell \geq 1$  we consider all patches of size  $N = 4 \times 2^\ell$  that can be built from patches of half size. Let  $\mathcal{G}_N$  be the set of centers of such patches:

$$\mathcal{G}_N = \left\{ \mathbf{p} \mid \mathbf{p} + \frac{N}{4} \mathbf{o}_i \in \mathcal{G}_{\frac{N}{2}}, i = 0, \dots, 3 \right\}. \quad (6)$$

For the sake of clarity, we define the short-hand notations for the correlation map of the quadrant  $i$  with an offset  $\frac{N}{4} \mathbf{o}_i$ :

$$C_i \left( \frac{N}{2}, \mathbf{p}' \right) := C_{\frac{N}{2}, \mathbf{p} + \frac{N}{4} \mathbf{o}_i} \left( \mathbf{p}' + \frac{N}{4} \mathbf{o}_i \right). \quad (7)$$

Let  $\Theta = \left\{ -\frac{N}{8}, \dots, \frac{N}{8} \right\} \times \left\{ -\frac{N}{8}, \dots, \frac{N}{8} \right\}$  be the domain over which we compute max-pooling scores. The computation of the score of the parent patch  $I_{N, \mathbf{p}}$  is given by:

$$C_{N, \mathbf{p}}(\mathbf{p}') = \frac{1}{4} \sum_{i=0}^3 \max_{\mathbf{m} \in \Theta} C_i \left( \frac{N}{2}, \mathbf{p}' + \mathbf{m} \right). \quad (8)$$

We now explain how  $C_{N, \mathbf{p}}$  can be computed efficiently by a succession of operators on the correlation maps. First, we notice that the larger a patch (*i.e.* after several iterations), the smaller the spatial variation of its correlation map (see Figure 4). This is due to the statistics of natural images, in which low frequencies significantly dominate over high frequencies. As a consequence, we integrate a subsampling step of factor 2 at each iteration, expressed with an operator  $\mathcal{S}$ :

$$\mathcal{S} : C(\mathbf{p}') \rightarrow C(2\mathbf{p}'). \quad (9)$$

The subsampling reduces by 4 the surface of the correlation maps and, as a direct consequence, the computational requirements. Furthermore, it makes the max-pooling domain  $\Theta$  become independent from  $N$  in the subsampled maps, as it exactly cancels out the effect of doubling  $N = 4 \times 2^\ell$  at each iteration. We call  $\mathcal{P}$  the max-pooling operator with fixed  $\Theta = \{-1, 0, 1\} \times \{-1, 0, 1\}$ :

$$\mathcal{P} : C(\mathbf{p}') \rightarrow \max_{\mathbf{m} \in \{-1, 0, 1\}^2} C(\mathbf{p}' + \mathbf{m}). \quad (10)$$

Similarly, the shift  $2^\ell \mathbf{o}_i$  applied to the correlation maps in Equation (7) becomes simply  $\mathbf{o}_i$  after subsampling. Let  $\mathcal{T}_t$  be the shift (or translation) operator on the correlation map:

$$\mathcal{T}_t : C(\mathbf{p}') \rightarrow C(\mathbf{p}' - \mathbf{t}). \quad (11)$$

Finally, we incorporate an additional non-linear mapping at each iteration by applying a power transform  $\mathcal{R}_\lambda$  (Malik and Perona 1990; LeCun et al 1998a):

$$\mathcal{R}_\lambda : C(\cdot) \rightarrow C(\cdot)^\lambda \quad (12)$$

This step, commonly referred to as rectification, is added in order to better propagate high correlations after each level, or, in other words, to counterbalance the fact that max-pooling tends to retain only high scores. Such post-processing is commonly used in deep convolutional networks (LeCun et al 1998b; Bengio 2009). In practice, good performance is obtained with  $\lambda \simeq 1.4$ , see Section 5. Equation (8) can thus be written as:

$$C_{N, \mathbf{p}} = \frac{1}{4} \sum_{i=0}^3 (\mathcal{R}_\lambda \circ \mathcal{T}_{\mathbf{o}_i} \circ \mathcal{S} \circ \mathcal{P}) \left( C_{\frac{N}{2}, \mathbf{p} + \frac{N}{4} \mathbf{o}_i} \right) \quad (13)$$

Figure 6 illustrates the computation of correlation maps for different patch sizes and Algorithm 1 summarizes our approach. The resulting set of correlation maps across iterations is referred to as multi-level correlation pyramid.

Note that Equation (8) implicitly defines the set of possible displacements of the approach, see Figure 2. Given the position of a parent patch, each child patch can move only within a small extent, equal to the quarter of its own size. Figure 4 shows the correlation maps for patches of size 4, 8 and 16. Clearly, correlation maps for larger patch gets more and more discriminative, while still allowing non-rigid matching.

---

#### Algorithm 1 Computing the multi-level correlation pyramid.

---

**Input:** Images  $I, I'$

**For**  $\mathbf{p} \in \mathcal{G}_4$  **do**

$$C_{4, \mathbf{p}} = I_{4, \mathbf{p}} \star I' \quad (\text{convolution, Eq. (4)})$$

$$C_{4, \mathbf{p}} \leftarrow \mathcal{R}_\lambda(C_{4, \mathbf{p}}) \quad (\text{rectification, Eq. (12)})$$

$N \leftarrow 4$

**While**  $N < \min(W, H)$  **do**

**For**  $\mathbf{p} \in \mathcal{G}_N$  **do**

$$C'_{N, \mathbf{p}} \leftarrow \mathcal{P}(C_{N, \mathbf{p}}) \quad (\text{max-pooling, Eq. (10)})$$

$$C'_{N, \mathbf{p}} \leftarrow \mathcal{S}(C'_{N, \mathbf{p}}) \quad (\text{sub-sampling, Eq. (9)})$$

$N \leftarrow 2N$

**For**  $\mathbf{p} \in \mathcal{G}_N$  **do**

$$C_{N, \mathbf{p}} = \frac{1}{4} \sum_{i=0}^3 \mathcal{T}_{\mathbf{o}_i} \left( C'_{\frac{N}{2}, \mathbf{p} + \frac{N}{4} \mathbf{o}_i} \right) \quad (\text{shifted average, Eq. (13)})$$

$$C_{N, \mathbf{p}} \leftarrow \mathcal{R}_\lambda(C_{N, \mathbf{p}}) \quad (\text{rectification, Eq. (12)})$$

**Return** the multi-level correlation pyramid  $\{C_{N, \mathbf{p}}\}_{N, \mathbf{p}}$

---

### 3.3 Top-down correspondence extraction

A score  $S = C_{N, \mathbf{p}}(\mathbf{p}')$  in the multi-level correlation pyramid represents the deformation-tolerant similarity of two patches  $I_{N, \mathbf{p}}$  and  $I'_{N, \mathbf{p}'}$ . Since this score is built from the similarity of 4 matching sub-patches at the previous pyramid level, we can thus recursively backtrack a set of correspondences to the first level (corresponding to matches of atomic patches). In this section,

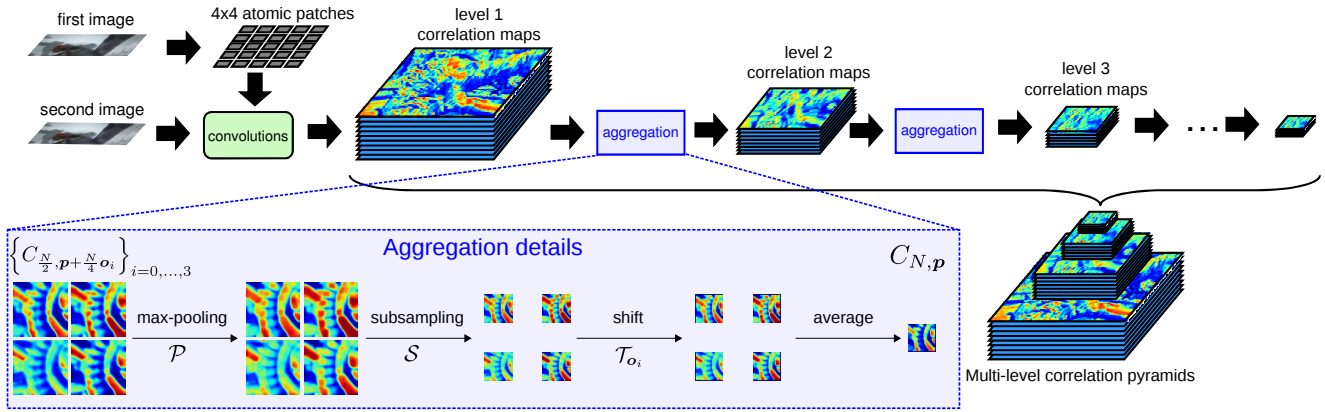


**Fig. 6** Computing the multi-level correlation pyramid. Starting with the level one correlation map, see Figure 3, it is iteratively aggregated to obtain the next levels. Aggregation consists of max-pooling, subsampling and computing a shifted average. The power transform is not included in the figure.

we first describe this backtracking. We, then, present the procedure for merging atomic correspondences backtracked from different entry points in the multi-level pyramid, which constitutes the final output of DeepMatching.

Compared to our initial version of DeepMatching (Weinzaepfel et al 2013), we have updated match scoring and entry point selection to optimize the execution time.

*Backtracking atomic correspondences.* Given an entry point  $C_{N, \mathbf{p}}(\mathbf{p}')$  in the pyramid (*i.e.* a match between two patches  $I_{N, \mathbf{p}}$  and  $I'_{N, \mathbf{p}'}$ <sup>1</sup>), we retrieve atomic correspondences by successively undoing the steps used to aggregate correlation maps during the pyramid construction, see Figure 7. The entry patch  $I_{N, \mathbf{p}}$  is itself composed of four moving quadrants  $I_{N, \mathbf{p}}^i$ ,  $i = 0 \dots 3$ . Due to the subsampling, the quadrant  $I_{N, \mathbf{p}}^i = I_{\frac{N}{2}, \mathbf{p} + \frac{N}{4} \mathbf{o}_i}$  matches with  $I_{\frac{N}{2}, 2(\mathbf{p}' + \mathbf{o}_i) + \mathbf{m}_i}$  where

$$\mathbf{m}_i = \arg \max_{\mathbf{m} \in \{-1, 0, 1\}^2} C_{\frac{N}{2}, \mathbf{p} + \frac{N}{4} \mathbf{o}_i}(2(\mathbf{p}' + \mathbf{o}_i) + \mathbf{m}). \quad (14)$$

For the sake of clarity, define the short-hand notations  $\mathbf{p}_i = \mathbf{p} + \frac{N}{4} \mathbf{o}_i$  and  $\mathbf{p}'_i = 2(\mathbf{p}' + \mathbf{o}_i) + \mathbf{m}_i$ . Let  $B$  be the function that assigns to a tuple  $(N, \mathbf{p}, \mathbf{p}', s)$ , representing a correspondence between pixel  $\mathbf{p}$  and  $\mathbf{p}'$  for patch of size  $N$  with a score  $s \in \mathbb{R}$ , the set of the correspondences of children patches:

$$B(N, \mathbf{p}, \mathbf{p}', s) = \begin{cases} \{(\mathbf{p}, \mathbf{p}', s)\} & \text{if } N = 4, \\ \left\{ \left( \frac{N}{2}, \mathbf{p}_i, \mathbf{p}'_i, s + C_{\frac{N}{2}, \mathbf{p}_i}(\mathbf{p}'_i) \right) \right\}_{i=0}^3 & \text{else.} \end{cases} \quad (15)$$

<sup>1</sup> Note that  $I'_{N, \mathbf{p}'}$  only roughly corresponds to a  $N \times N$  square patch centered at  $2^l \mathbf{p}'$  in  $I'$ , due to subsampling and possible deformations.

Given a set  $\mathcal{M}$  of such tuples, let  $\mathcal{B}(\mathcal{M})$  be the union of the sets  $B(c)$  for all  $c \in \mathcal{M}$ . Note that if all candidate correspondences  $c \in \mathcal{M}$  corresponds to atomic patches, then  $\mathcal{B}(\mathcal{M}) = \mathcal{M}$ .

Thus, the algorithm for backtracking correspondences is the following. Consider an entry match  $\mathcal{M} = \{(N, \mathbf{p}, \mathbf{p}', C_{N, \mathbf{p}}(\mathbf{p}'))\}$ . We repeatedly apply  $\mathcal{B}$  on  $\mathcal{M}$ . After  $\mathfrak{N} = \log_2(N/4)$  calls, we get one correspondence for each of the  $2^{2\mathfrak{N}}$  atomic patches. Furthermore, their score is equal to the sum of all patch similarities along their backtracking path.

*Merging correspondences.* We have shown how to retrieve atomic correspondences from a match between two deformable (potentially large) patches. Despite this flexibility, a single match is unlikely to explain the complex set of motions that can occur in pair of video frames. For instance, the case of two objects moving independently with significantly different motions exceeds the deformation range of DeepMatching (we quantitatively specify this range in the next subsection).

We thus merge atomic correspondences gathered from different entry points (matches) in the pyramid. In the initial version of DeepMatching (Weinzaepfel et al 2013), entry points were local maxima over all correlation maps. This was replaced by a faster procedure, that starts with all possible matches in the last pyramid level (*i.e.*  $\mathcal{M} = \{(N, \mathbf{p}, \mathbf{p}', C_{N, \mathbf{p}}(\mathbf{p}')) | N = N_{\max}\}$ ). Using this level only represents significantly less entry points than starting from all maxima in the entire pyramid. We did not observe any impact on the matching performance. Because  $\mathcal{M}$  contains a lot of overlapping patches, most of the computation during repeated calls to  $\mathcal{M} \leftarrow \mathcal{B}(\mathcal{M})$  can be factorized. In other words, as soon as two tuples in  $\mathcal{M}$  are equal in terms of  $N$ ,  $\mathbf{p}$  and  $\mathbf{p}'$ , the one with the lowest score is simply eliminated. We thus obtain a



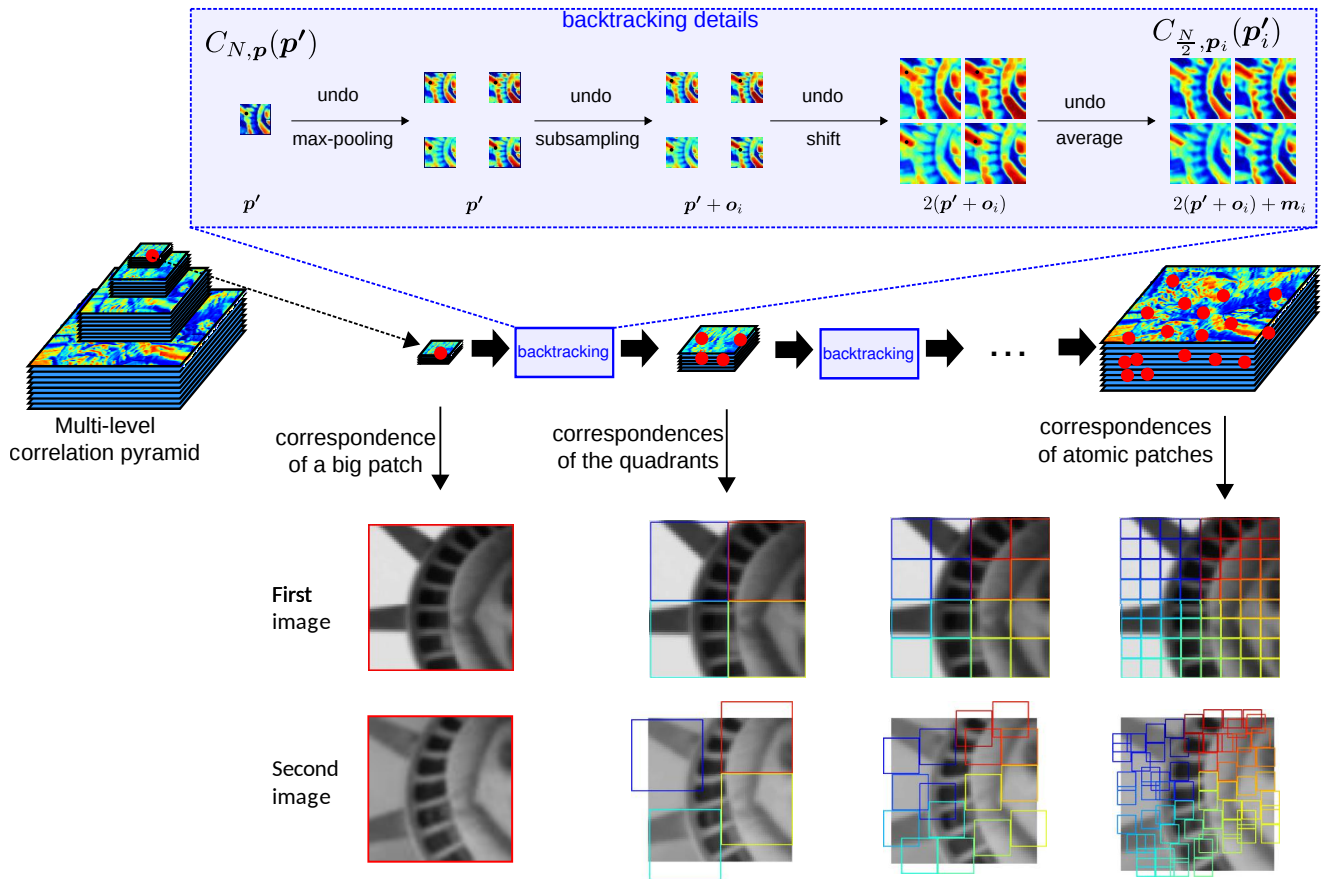


**Fig. 7** Backtracking atomic correspondences from a score in the pyramid. Given a score (red dot) in the pyramid (left), we apply the backtracking procedure, which consists of undoing the aggregation done previously (top), to get scores at lower level until the first is reached. In more detail, the top shows how from a position  $\mathbf{p}'$  in  $C_{N, \mathbf{p}'}(\mathbf{p}')$ , we retrieve the positions of the 4 quadrants  $\mathbf{p}'_i = 2(\mathbf{p}' + \mathbf{o}_i) + \mathbf{m}_i$  in  $C_{\frac{N}{2}, \mathbf{p}_i}(\mathbf{p}'_i)$ . Black dots on the correlation maps in the backtracking details show the position on the correlation maps. While score at high level corresponds to match of parent patch (bottom left), the scores at the previous level corresponds to match for its 4 quadrants. Finally, the set of scores at the first level corresponds to matches of atomic patches.

set of atomic correspondences  $\mathcal{M}'$ :

$$\mathcal{M}' = (\mathcal{B} \circ \dots \circ \mathcal{B})(\mathcal{M}) \quad (16)$$

that we filter with reciprocal match verification. The final set of correspondences  $\mathcal{M}''$  is obtained as:

$$\mathcal{M}'' = \{(\mathbf{p}, \mathbf{p}', s) \mid \text{BestAt}(\mathbf{p}) = \text{BestAt}'(\mathbf{p}')\}_{(\mathbf{p}, \mathbf{p}', s) \in \mathcal{M}'} \quad (17)$$

where  $\text{BestAt}(\mathbf{p})$  (resp.  $\text{BestAt}'(\mathbf{p}')$ ) returns the best match in a small vicinity of  $4 \times 4$  pixels around  $\mathbf{p}$  in the first image (resp. around  $\mathbf{p}'$  in the second image) from  $\mathcal{M}'$ .

### 3.4 Discussion and Analysis of DeepMatching

*Multi-size patches and repetitive textures.* During the bottom-up pass of the algorithm, we iteratively aggregate correlation maps of smaller patches to form the

correlation maps of larger patches. Doing so, we effectively consider patches of different sizes ( $4 \times 2^\ell$ ,  $\ell \geq 0$ ), in contrast to most existing matching methods. This is a key feature of our approach when dealing with repetitive textures. As one moves up to coarser levels, the matching problem gets less ambiguous. Larger patches get more credit, and our method can correctly match repetitive patterns. Figures 8 illustrates this property.

*Quasi-dense correspondences.* Our method retrieves dense correspondences from every single match between large regions (*i.e.* entry point for the backtracking in the top-level correlation maps), even in weakly textured areas; this is in contrast to single correspondences obtained when matching pairs of descriptors (*e.g.* SIFT). Quantitative assessment, by comparing the density of matches obtained from several matching schemes, is given in Section 5.

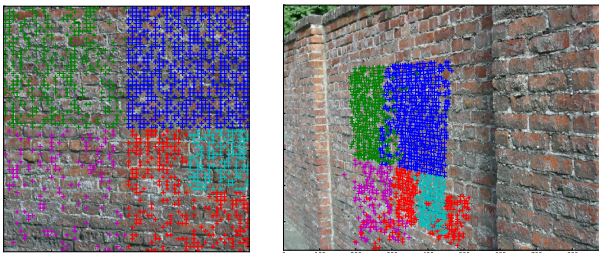


**Fig. 8** Matching result between two images with repetitive textures. Each color refers to correspondences obtained from a different entry point in the correlation pyramid.

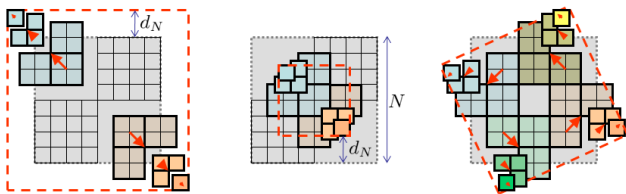


**Fig. 9** Extent of the tolerance of DeepMatching to deformations. From left to right: up-scale of 1.5x, down-scale of 0.5x, rotation of  $26^\circ$ . The gray (resp. red) dashed square represents the patch in the reference (resp. target) image. For clarity, only the corner pixels are maximally deformed.

*Non-rigid deformations.* Our matching algorithm is able to cope with various sources of image deformations: object-induced or camera-induced. The set of feasible deformations, explicitly defined by Equation (8), theoretically allows to deal with a scaling factor in the range  $[\frac{1}{2}, \frac{3}{2}]$  and rotations roughly in the range  $[-26^\circ, 26^\circ]$ . Note also that DeepMatching is translation-invariant by construction, thanks to the convolutional nature of the processing.

*Proof* Given a patch of size  $N = 4 \times 2^\ell$  located at level  $\ell \geq 1$ , Equation (8) allows each of its children patches to move by at most  $N/8$  pixels from their ideal location. By recursively summing the displacements at each level, we find the maximal displacements for an atomic patch to be  $d_N = \sum_{i=1}^{\ell} 2^{i-1} = 2^\ell - 1$ . An example is given in Figure 9 with  $N = 32$  and  $\ell = 3$ . Relatively to  $N$ , we thus have  $\lim_{N \rightarrow \infty} (N + 2d_N)/N = \frac{3}{2}$  and  $\lim_{N \rightarrow \infty} (N - 2d_N)/N = \frac{1}{2}$ . For a rotation, the rationale is similar, see Figure 9.  $\square$

*Built-in smoothing.* Furthermore, correspondences generated through backtracking of a single entry point in the correlation maps are naturally smooth. Indeed, feasible deformations (or warpings) cannot be too “far” from the identity warping. Figure 10 illustrates this, by comparing the smoothness of warpings sampled from

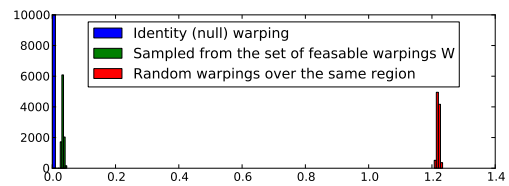


**Fig. 10** Histogram of the per-pixel averaged smoothness (computed from Eq. 20) of 10,000 warpings randomly sampled from the set of feasible warpings for patch of size  $128 \times 128$  and the set of random warpings over the same region. The identity warping has a smoothness of 0.

the set of allowed deformation with initial patches of size  $128 \times 128$  with random warpings of atomic patches. Clearly, they are different by orders of magnitude.

#### *Relation to Deep Convolutional Neural Networks (CNNs).*

Since DeepMatching is multi-layer, convolutional, and nonlinear, it is somewhat akin to deep CNNs (LeCun et al 1998a). In the following we describe how it stands in contrast to standard deep CNN architectures. Deep networks would learn from data a feature representation using multi-layer, convolutional, nonlinear, architecture, and would then compare two images based on their respective feature representations using some (Euclidean) similarity measure. In contrast to deep network approaches, DeepMatching does not learn any feature representation from the data. Instead, DeepMatching directly computes spatial correlation maps corresponding to local convolutional matching at the patch level. The algorithm then propagates up matching information in the (locally re-optimized) hierarchy using rectifying stages in between each layer. In fact, DeepMatching effectively defines a similarity measure between two images.

*Time and space complexity.* DeepMatching has a complexity  $O(LL')$  in memory and time, where  $L = WH$  and  $L' = W'H'$  are the number of pixels of each image.

*Proof* Computing the initial convolutions is a  $O(LL')$  operation. Then, at each level of the pyramid, the process is repeated while the complexity is divided by a factor 4 due to the subsampling step in the target image (since the cardinality of  $|\{\mathcal{G}_N\}|$  remains approximately constant). Thus, the total complexity of the correlation maps computation is, at worst,  $O(\sum_{n=0}^{\infty} LL'/4^n) = O(LL')$ . During the top-down pass, most backtracking paths can be pruned as soon as they cross a concurrent path with a higher score (see Section 3.3). Thus, all correlations will be examined at most once, and there are  $\sum_{n=0}^{\infty} LL'/4^n$  values in total. However, this analysis is worst-case. In practice, only correlations lying on maximal paths are actually examined.  $\square$

## 4 Extensions of DeepMatching

### 4.1 Approximate DeepMatching

As a consequence of its  $O(LL')$  space complexity, DeepMatching requires an amount of RAM that is orders of magnitude above other state-of-the-art matching methods. This could correspond to several gigabytes for images of moderate size ( $800 \times 600$  pixels); see experiments. This section introduces an approximation of DeepMatching that allows to trade off matching quality for reduced time and memory usage. As shown in the experiments, near-optimal results can be obtained at a fraction of the original cost.

Our approximation proposes to compress the representation of atomic patches  $\{I_{4,p}\}$ . Atomic patches carry little information, and thus are highly redundant. For instance, in uniform regions, all patches are nearly identical (*i.e.*, gradient-wise). To exploit this property, we index atomic patches with a small set of patch prototypes. Specifically, we substitute each patch with its closest neighbor in a fixed dictionary of  $D$  prototypes. Hence, we need to perform and store only  $D$  convolutions at the first level, instead of  $O(L)$  (with  $D \ll O(L)$ ). This drastically reduces both memory and time complexity. Note that higher pyramid levels also benefit from this optimization. Indeed, two parent patches at the second level get the exact same correlation map whenever their children are assigned the same prototypes (and thus the same correlation maps). The same reasoning in fact also holds at all subsequent levels, but the gains rapidly diminish due to statistical unlikelihood of the required condition. This is not really an issue, since the memory and computational cost mostly occurs on the initial levels; see Sec. 3.4.

In practice, we build the prototype dictionary using k-means, as it is specifically designed to minimize the approximation error between input descriptors and resulting centroids (*i.e.* prototypes). Given a pair of images to match, we perform on-line clustering of all descriptors of atomic patches  $\{I_{4,p}\} = \{\mathbf{R}\}$  in the first image. Since original descriptors belong to an hypersphere (each pixel descriptor  $\mathbf{R}_{i,j}$  has norm 1, thus  $\|\mathbf{R}\| = 16$ ), we modify the k-means procedure so as to project the estimated centroids on the hypersphere at each iteration. We find experimentally that this is important to obtain good results.

### 4.2 Scale and rotation invariant DeepMatching

For a variety of tasks, objects to be matched can appear under image rotations or at different scales [Lowe \(2004\)](#); [Mikolajczyk et al \(2005\)](#); [Szeliski \(2010\)](#); [HaCohen et al](#)

[\(2011\)](#). As discussed above, DeepMatching (DM) is only invariant to moderate rescaling and rotations. We now present a fully invariant version of DM.

The approach is straightforward: we apply DM to several rotated and rescaled versions of the second image. According to the invariance range of DM, we use steps of  $\pi/4$  for image rotation and power of  $\sqrt{2}$  for scale changes. While iterating over all combinations of scale changes and rotations, we maintain a list  $\mathcal{M}'$  of all atomic correspondences obtained so far, *i.e.* corresponding positions and scores. As before, the final output correspondences consists of the reciprocal matches in  $\mathcal{M}'$ . Storing all matches and finally choosing the best ones based on reciprocal verification permits to capture distinct motions possibly occurring together in the same scene (*e.g.* one object could have rotated, while the rest of the scene did not move). The steps of the approach are described in [Algorithm 2](#).

Since we iterate sequentially over a fixed list of rotations and scale changes, the space and time complexity of the algorithm remains unchanged (*i.e.*  $O(LL')$ ). In practice, the run-time compared to DM is multiplied by a constant approximately equal to 70, see [Section 5](#). Note that the algorithm admits a straightforward parallelization.

---

**Algorithm 2** Scale and rotation invariant version of DeepMatching (DM).  $I_\sigma$  denotes the image  $I$  downsized by a factor  $\sigma$ , and  $\mathcal{R}_\theta$  denotes rotation by an angle  $\theta$ .

---

**Input:**  $I, I'$  are the images to be matched  
**Initialize** an empty set  $\mathcal{M}' = \{\}$  of correspondences  
**For**  $\sigma \in \{-2, -1.5, \dots, 1.5, 2\}$  **do**  
 $\sigma_1 \leftarrow \max(1, 2^{+\sigma})$  # either downsize image 1  
 $\sigma_2 \leftarrow \max(1, 2^{-\sigma})$  # or downsize image 2  
**For**  $\theta \in \{0, \frac{\pi}{4}, \dots, \frac{7\pi}{4}\}$  **do**  
 # get raw atomic correspondences (eq. (16))  
 $\mathcal{M}'_{\sigma,\theta} \leftarrow \text{DeepMatching}(I_{\sigma_1}, \mathcal{R}_{-\theta} * I'_{\sigma_2})$   
 # Geometric rectification to the input image space:  
 $\mathcal{M}'_{\sigma,\theta}^R \leftarrow \{(\sigma_1 \mathbf{p}, \sigma_2 \mathcal{R}_\theta \mathbf{p}', s) \mid \forall (\mathbf{p}, \mathbf{p}', s) \in \mathcal{M}'_{\sigma,\theta}\}$   
 # Concatenate results:  
 $\mathcal{M}' \leftarrow \mathcal{M}' \cup \mathcal{M}'_{\sigma,\theta}^R$   
 $\mathcal{M}'' \leftarrow \text{reciprocal}(\mathcal{M}')$  # keep reciprocal matches (eq. (17))  
**Return**  $\mathcal{M}''$

---

### 4.3 DeepFlow

We now present our approach for optical flow estimation, DeepFlow, that blends the DeepMatching algorithm into an energy minimization framework. We follow a line of thought similar to [Brox and Malik \(2011\)](#). We make four additions: (i) we incorporate the DeepMatching algorithm as matching component; (ii) we

add a normalization in the data term to downweight the impact of locations with high spatial image derivatives; (iii) we use a different weight at each level to downweight the matching term at finer scales; and (iv) the smoothness term is locally weighted. Let  $I_1, I_2 : \Omega \rightarrow \mathbb{R}^c$  be two consecutive images defined on  $\Omega$  with  $c$  channels. The goal is to estimate the flow  $\mathbf{w} = (u, v)^\top : \Omega \rightarrow \mathbb{R}^2$ . We assume that the images are already smoothed using a Gaussian filter of standard deviation  $\sigma$ . The energy we optimize is a weighted sum of a data term  $E_D$ , a smoothness term  $E_S$  and a matching term  $E_M$ :

$$E(\mathbf{w}) = \int_{\Omega} E_D + \alpha E_S + \beta E_M d\mathbf{x} \quad (18)$$

For the three terms, we use a robust penalizer  $\Psi(s^2) = \sqrt{s^2 + \epsilon^2}$  with  $\epsilon = 0.001$  which has shown excellent results (Sun et al 2014b).

*Data term.* The data term is a separate penalization of the color and gradient constancy assumptions with a normalization factor as in Zimmer et al (2011). We start from the optical flow constraint assuming the brightness constancy:  $(\nabla_3^\top I)\mathbf{w} = 0$  with  $\nabla_3 = (\partial_x, \partial_y, \partial_t)^\top$  the spatio-temporal gradient. A basic way to build a data term is to penalize it, *i.e.*  $E_D = \Psi(\mathbf{w}^\top \mathbf{J}_0 \mathbf{w})$  with  $\mathbf{J}_0$  the tensor defined by  $\mathbf{J}_0 = (\nabla_3 I)(\nabla_3^\top I)$ . As highlighted by Zimmer et al (2011), such a data term adds a higher weight in locations corresponding to high spatial image derivatives. We normalize it by the norm of the spatial derivatives plus a small factor to avoid division by zero, and to reduce a bit the influence in tiny gradient locations (Zimmer et al 2011). Let  $\bar{\mathbf{J}}_0$  be the normalized tensor  $\bar{\mathbf{J}}_0 = \theta_0 \mathbf{J}_0$  with  $\theta_0 = (\|\nabla_2 I\|^2 + \zeta^2)^{-1}$ . We set  $\zeta = 0.1$  in the following. To deal with color images, we consider the tensor defined for a channel  $i$  denoted by upper indices  $\bar{\mathbf{J}}_0^i$  and we penalize the sum over channels:  $\Psi(\sum_{i=1}^c \mathbf{w}^\top \bar{\mathbf{J}}_0^i \mathbf{w})$ . We consider images in the RGB color space.

We separately penalize the gradient constancy assumption (Bruhn et al 2005). Let  $I_x$  and  $I_y$  be the derivatives of the images with respect to the  $x$  and  $y$  axis respectively. Let  $\bar{\mathbf{J}}_{xy}^i$  be the tensor for the channel  $i$  including the normalization

$$\bar{\mathbf{J}}_{xy}^i = (\nabla_3 I_x^i)(\nabla_3^\top I_x^i) / (\|\nabla_2 I_x^i\|^2 + \zeta^2) + (\nabla_3 I_y^i)(\nabla_3^\top I_y^i) / (\|\nabla_2 I_y^i\|^2 + \zeta^2).$$

The data term is the sum of two terms, balanced by two weights  $\delta$  and  $\gamma$ :

$$E_D = \delta \Psi \left( \sum_{i=1}^c \mathbf{w}^\top \bar{\mathbf{J}}_0^i \mathbf{w} \right) + \gamma \Psi \left( \sum_{i=1}^c \mathbf{w}^\top \bar{\mathbf{J}}_{xy}^i \mathbf{w} \right) \quad (19)$$

*Smoothness term.* The smoothness term is a robust penalization of the gradient flow norm:

$$E_S = \Psi (\|\nabla u\|^2 + \|\nabla v\|^2) \quad (20)$$

The smoothness weight  $\alpha$  is locally set according to image derivatives (Wedel et al 2009). We use the same weight as Xu et al (2012):  $\alpha(\mathbf{x}) = \exp(-\kappa \nabla_2 I(\mathbf{x}))$ .

*Matching term.* The matching term encourages the flow estimation to be similar to a precomputed vector field  $\mathbf{w}'$ . To this end, we penalize the difference between  $\mathbf{w}$  and  $\mathbf{w}'$ , using the robust penalizer  $\Psi$ . Since the matching is not totally dense, we add a binary term  $c(\mathbf{x})$  which is equal to 1 if and only if a match is available at  $\mathbf{x}$ .

We also multiply each matching penalization by a weight  $\phi(\mathbf{x})$ , which must be low in flat regions or when matches look false. To this end, we call  $\lambda(\mathbf{x})$  the minimum eigenvalue of the autocorrelation matrix multiplied by 10. We also compute  $\Delta(\mathbf{x}) = \sum_{i=1}^c |I_1^i(\mathbf{x}) - I_2^i(\mathbf{x} - \mathbf{w}'(\mathbf{x}))| + |\nabla I_1^i(\mathbf{x}) - \nabla I_2^i(\mathbf{x} - \mathbf{w}'(\mathbf{x}))|$ . We then compute the score  $\phi$  as a Gaussian kernel on  $\Delta$  weighted by  $\lambda$  with a parameter  $\sigma_M$ , experimentally set to  $\sigma_M = 50$ . More precisely, we define  $\phi(\mathbf{x})$  at each point  $\mathbf{x}$  with a match  $\mathbf{w}'(\mathbf{x})$  as:

$$\phi(\mathbf{x}) = \sqrt{\tilde{\lambda}(\mathbf{x})} / (\sigma_M \sqrt{2\pi}) \exp(-\Delta(\mathbf{x}) / 2\sigma_M).$$

The matching term is then  $E_M = c\phi\Psi(\|\mathbf{w} - \mathbf{w}'\|^2)$ .

*Minimization.* This energy objective is non-convex and non-linear. To solve it, we use a similar numerical optimization algorithm as Brox et al (2004). An incremental coarse-to-fine warping strategy is used with a downsampling factor  $\eta = 0.95$ . The remaining equations are still non-linear due to the robust penalizers. We apply 5 inner fixed point iterations where the non-linear weights and the flow increments are iteratively updated while fixing the other. To approximate the solution of the linear system, we use 25 iterations of the Successive Over Relaxation (SOR) method.

To downweight the matching term on fine scales, we use a different weight  $\beta^k$  at each level as proposed by Stoll et al (2012). We set  $\beta^k = \beta(k/k_{\max})^b$  where  $b$  is a parameter of the flow,  $k$  the current level of computation and  $k_{\max}$  the number of the coarsest level.

## 5 Experiments

This section presents an experimental evaluation of Deep-Matching and DeepFlow. The datasets and metrics used to evaluate DeepMatching and DeepFlow are introduced

in Section 5.1. Experimental results for DeepMatching and DeepFlow are given in Sections 5.2 and 5.3 respectively.

## 5.1 Datasets and metrics

In this section we briefly introduce the matching and flow datasets used in our experiments. Since consecutive frames of a video are well-suited to evaluate a matching approach, we use several optical flow datasets for evaluating both the quality of matching and flow, but rely on different metrics.

*The Mikolajczyk dataset* was originally proposed by Mikolajczyk et al (2005) to evaluate and compare the performance of keypoint detectors and descriptors. It is one of the standard benchmarks for evaluating matching approaches. The dataset consists of 8 sequences of 6 images each viewing a scene under different conditions, such as illumination changes or viewpoint changes. The images of a sequence are related by homographies. During the evaluation, we comply to the standard procedure in which the first image of each scene is matched to the 5 remaining ones. Since our goal is to study robustness of DeepMatching to geometric distortions, we follow HaCohen et al (2011) and restrict our evaluation to the 4 most difficult sequences with viewpoint changes: *bark*, *boat*, *graf* and *wall*.

*The MPI-Sintel dataset* (Butler et al 2012) is a challenging evaluation benchmark for optical flow estimation, constructed from realistic computer-animated films. The dataset contains sequences with large motions and specular reflections. In the training set, more than 17.5% of the pixels have a motion over 20 pixels, approximately 10% over 40 pixels. We use the “final” version, featuring rendering effects such as motion blur, defocus blur and atmospheric effects. For our flow experiments, we split the original training set into a “small” training set (20%) and a validation set (80%) for which we report results. Note that annotations for the test set are not publicly available.

*The Middlebury dataset* (Baker et al 2011) has been extensively used for evaluating optical flow methods. The dataset contains complex motions, but most of the motions are small. Less than 3% of the pixels have a motion over 20 pixels, and no motion exceeds 25 pixels (training set).

*The Kitti dataset* Geiger et al (2013) contains real-world sequences taken from a driving platform. The dataset includes non-Lambertian surfaces, different lighting conditions, a large variety of materials and large displacements. More than 16% of the pixels have motion over 20 pixels.

*Performance metric for matching.* Choosing a performance measure for matching approaches is delicate. Matching approaches typically do not return dense correspondences, but output varying numbers of matches for the same image pair. Furthermore, matching patches might be concentrated in different areas of the image.

Most matching approaches, including DeepMatching, are based on establishing correspondences between patches. Given a pair of matching patches, it is possible to obtain a list of pixel correspondences for all pixels composing the patches. We, now, introduce an objective measure based on the number of correctly matched pixels compared to the overall number of pixels. We define “accuracy@ $T$ ” as the proportion of “correct” pixels from the first image with respect to the total number of pixels. A pixel is considered correct if its pixel match in the second image is closer than  $T$  pixels to ground-truth. In practice, we use a threshold of  $T = 10$  pixels, as it represents a sufficiently precise estimation (about 1% of image diagonal for all datasets), while allowing some tolerance in blurred areas that are difficult to match exactly. If a pixel belongs to several matches, we choose the one with the highest score to predict its correspondence. Pixels which do not belong to any patch have an infinite error.

*Performance metric for optical flow.* To evaluate optical flow, we follow the standard protocol and measure the average endpoint error over all pixels, denoted as “AEE”. The “s10-40” variant measures the AEE only for pixels with a ground-truth displacement between 10 and 40 pixels, and likewise for “s0-10” and “s40+”. In all cases, scores are averaged over all image pairs to yield the final result for a given dataset.

## 5.2 Matching Experiments

In this section we evaluate DeepMatching (DM). We present results for all datasets presented above but Middlebury, which does not feature long-range motions, the main difficulty in image matching. When evaluating on the Mikolajczyk dataset, we employ the scale and rotation invariant version of DM presented in Section 4.2.

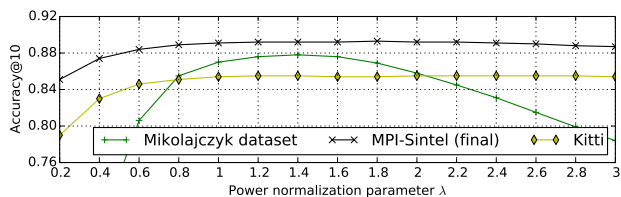


Fig. 11 Impact of the non-linear response rectification (eq. (12)).

### 5.2.1 Impact of the $\lambda$ parameter

We, first, evaluate the impact of the parameter  $\lambda$  of the non-linear rectification obtained by applying power normalization in eq. (12). Figure 11 displays the accuracy@10 for various values of  $\lambda$ . We can observe that the optimal performance is achieved at  $\lambda = 1.4$  for all datasets. We use this value in the remainder of our experiments.

### 5.2.2 Approximate DeepMatching

We now evaluate the performance of approximate DeepMatching (Section 4.1) and report its run-time and memory usage. We evaluate and compare two different ways of reducing the computational load. The first one simply consists in downsizing the input images, and upscaling the resulting matches accordingly. The second option is the compression scheme proposed in Section 4.1.

We evaluate both schemes jointly by varying the input image size (expressed as a fraction  $R$  of the original resolution) and the size  $D$  of the prototype dictionary (*i.e.* parameter of k-means in Section 4.1). We display the results in terms of matching accuracy against memory consumption in Figure 12 and as a function of  $D$  in Figure 13. Figure 12 shows that DeepMatching can be computed in an approximate manner for any given memory budget. Unsurprisingly, too low settings (*e.g.*  $R \leq 1/8$ ,  $D \leq 64$ ) result in a strong loss of performance. It should be noted that that we were unable to compute DeepMatching at full resolution ( $R = 1$ ) for  $D > 64$ , as the memory consumption explodes. As a consequence, all subsequent experiments in the paper are done at  $R = 1/2$ . In Figure 13, we observe that good trades-off are achieved for dictionary sizes comprised in  $D \in [64, 1024]$ . For instance, on MPI-Sintel, at  $D = 1024$ , 94% of the performance of the uncompressed case ( $D = \infty$ ) is reached for half the computation time and one third of memory usage. The overhead of computing the dictionary prototypes with k-means is negligible, with the exception of the largest dictionary size ( $D = 4096$ ) for which it induces a slightly longer run-time than in the uncompressed case. Overall, the

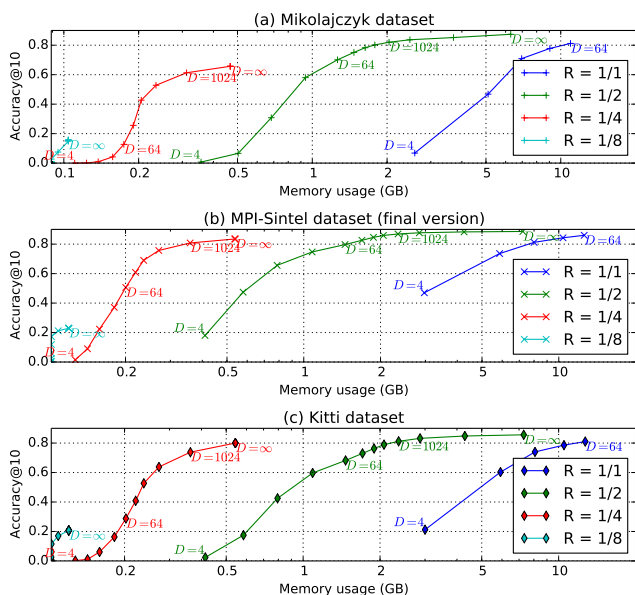


Fig. 12 Trade-off between memory consumption and matching performance for the different datasets. Memory usage is controlled by changing image resolution  $R$  (different curves) and dictionary size  $D$  (curve points).

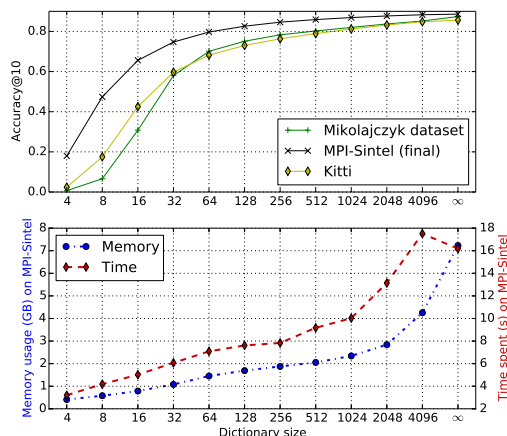


Fig. 13 Performance, memory usage and run-time for different levels of compression corresponding to the size  $D$  of the prototype dictionary (we set the image resolution to  $R = 1/2$ ). A dictionary size  $D = \infty$  stands for no compression.

proposed method for approximating DeepMatching is highly effective.

### 5.2.3 Comparison to the state of the art

We compare DM with several baselines and state-of-the-art matching algorithms, namely:

- SIFT keypoints extracted with DoG detector (Low 2004) and matched with FLANN (Muja and Lowe 2009), referred to as SIFT-NN,

Method	Mikolajczyk		MPI-Sintel (final)		Kitti	
	#	density	#	density	#	density
SIFT-NN	2084	0.59	836	0.25	1299	0.38
HOG-NN	-	-	4576	0.39	4293	0.34
KPM	-	-	446K	1	462K	1
GPM	545K	1	446K	1	462K	1
NRDC	545K	1	446K	1	462K	1
DM (ours)	3120	0.81	5920	0.96	5357	0.88

**Table 1** Statistics of the different matching methods. The “#” column refers to the average number of matches per image, and the density to the proportion of points on a regular grid with 10 pixel spacing that have a match within a 10px neighborhood.

- dense HOG matching, followed by nearest-neighbor matching with reciprocal verification as done in LDOF (Brox and Malik 2011), referred to as HOG-NN,
- Generalized PatchMatch (GPM) (Barnes et al 2010), with default parameters, 32x32 patches and 20 iterations (best settings in our experiments),
- Kd-tree PatchMatch (KPM) (Sun 2012), an improved version of PatchMatch based on better patch descriptors and Kd-trees optimized for correspondence propagation,
- Non-Rigid Dense Correspondences (NRDC) (HaCohen et al 2011), an improved version of GPM based on a multiscale iterative expansion/contraction strategy.

SIFT-NN, HOG-NN and DM output sparse matches, whereas GPM, KPM and NRDC output dense correspondence fields. SIFT keypoints, GPM and NRDC are scale and rotation invariant, whereas HOG-NN and KPM are not. We, therefore, do not report results for HOG-NN and KPM on the Mikolajczyk dataset which includes image rotations and scale changes.

Statistics about each method (average number of matches per image and their density) are reported in Table 1. Density is computed as the proportion of points on a regular grid with 10 pixel spacing that have a match in a 10 pixel neighborhood. This indicates how well matches “cover” the image. Table 1 shows that DeepMatching outputs 2 to 7 times more matches than SIFT-NN, and a comparable number to HOG-NN. Yet, the density for DM matches is much higher than for HOG-NN and SIFT-NN. This shows that DM matches are well distributed over the entire image, which is not the case for HOG-NN and SIFT-NN, as they have difficulties estimating matches in regions with weak or repetitive textures.

Quantitative results are listed in Table 2, and qualitative results in Figures 14, 15 and 16. Overall, DM significantly outperforms all other methods, even when reduced settings are used (*e.g.* for image resolution  $R = 1/2$  and  $D = 1024$  prototypes). A comparison with a preliminary version of DeepMatching Weinzaepfel et al (2013), denoted as DM\*, is also provided. This one

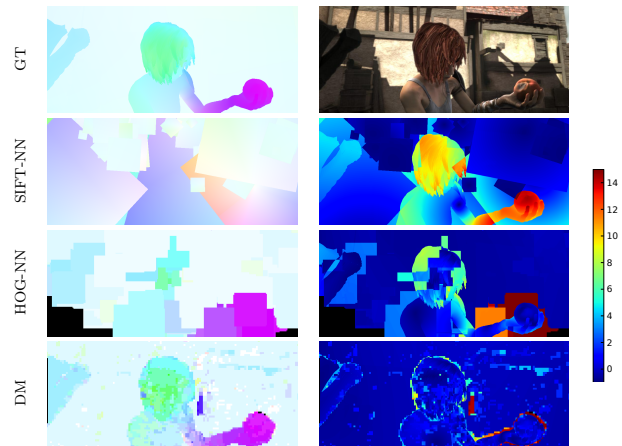


**Fig. 15** Example of matching results on MPI-Sintel (pixel displacements have been inferred from matching patches). Left: ground-truth (top) and predicted motion maps for SIFT-NN, HOG-NN and DM. Right: corresponding error maps. SIFT-NN and HOG-NN patches result in too coarse motion estimates.

is significantly outperformed by the current version in terms of accuracy, memory and time thanks to a more efficient scoring scheme (Section 3.3). As expected, SIFT-NN performs rather well in presence of global image transformation (Mikolajczyk dataset), but yields the worst result for the case of more complex motions (flow datasets). Figure 15 illustrate the reason: SIFT’s large patches are way too coarse to follow motion boundaries precisely. The same issue also holds for HOG-NN. Methods predicting dense correspondence fields (KPM, GPM) return a finer estimate, but are not robust to repetitive textures (Figure 16) as they rely on weakly discriminative small patches. As for DM and NRDC, they avoid this issue thanks to using multi-size non-rigid patches (for DM) and multiple iterations of an expansion/contraction strategy (for NRDC). This latter method nevertheless gets significantly outperformed by DM on the Mikolajczyk dataset, see Figure 14.

In terms of computing resources, DeepMatching with full settings ( $R = 1/2$ ,  $D = \infty$ ) is by far the most costly method. The scale and rotation invariant version of DM, used for the Mikolajczyk dataset, is slow compared to other approaches, due to its sequential processing (*i.e.* treating each combination of a rotation and a scaling factor one after the other), yet yields near perfect results. However, running DM with reduced settings is very competitive to the other approaches. On MPI-Sintel and Kitti, for instance, DM with a quarter resolution has a run time comparable to the fastest method, SIFT-NN, with a reasonable memory usage, while still outperforming all methods in terms of accuracy@10 measure.

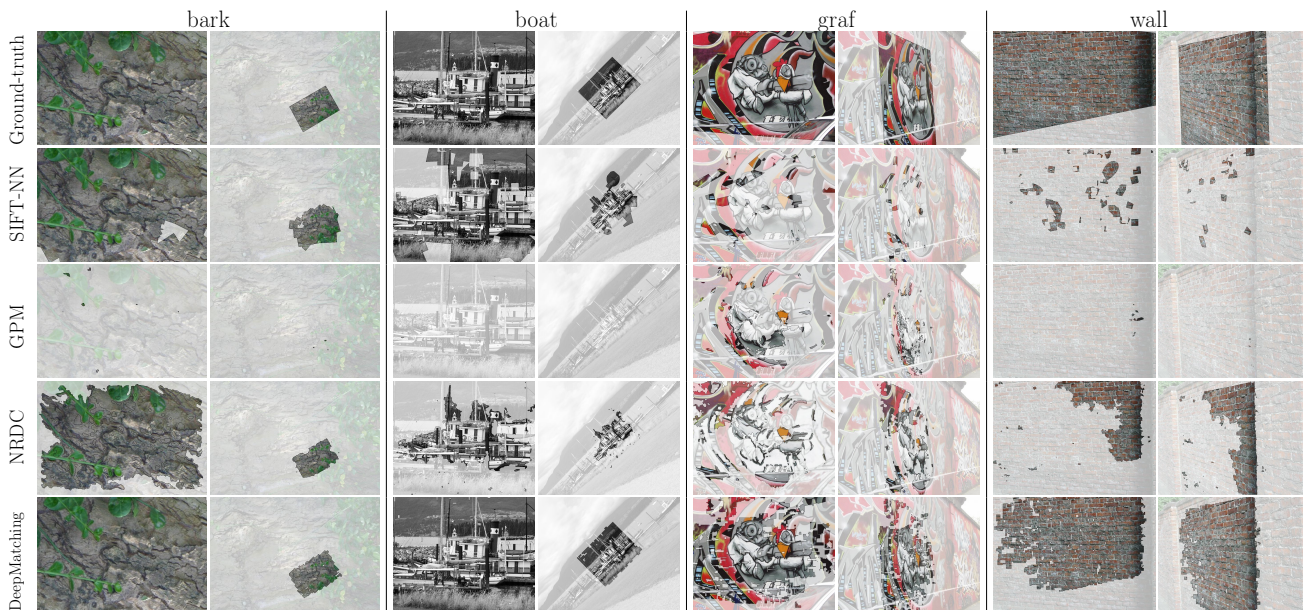


**Fig. 14** Comparison of matching results of different methods on the Mikolajczyk dataset. Each row shows pixels with correct correspondences for different methods (from top to bottom: ground-truth, SIFT-NN, GPM, NRDC and DM). For each scene, we select two images to match and fade out regions which are unmatched, *i.e.* those for which the matching error is above 15px or can not be matched. DeepMatching outperforms the other methods, especially on difficult cases like *graf* and *wall*.

method	$R$	$D$	accuracy@10	memory usage	matching time
<b>Mikolajczyk dataset</b>					
SIFT-NN			0.674	0.2 GB	1.4 s
GPM			0.303	0.1 GB	2.4 min
NRDC			0.692	0.1 GB	2.5 min
DM	1/4	$\infty$	0.657	0.5 GB	1.1 min
DM	1/2	1024	0.820	1.9 GB	5.8 min
DM	1/2	$\infty$	<b>0.878</b>	5.7 GB	8.1 min
<b>MPI-Sintel dataset (final)</b>					
SIFT-NN			0.684	0.2 GB	2.7 s
HOG-NN			0.712	3.4 GB	32 s
KPM			0.738	0.3 GB	7.3 s
GPM			0.812	0.1 GB	1.1 min
DM	1/4	$\infty$	0.835	0.5 GB	2.9 s
DM	1/2	1024	0.869	2.3 GB	10 s
DM	1/2	$\infty$	<b>0.892</b>	7.2 GB	16 s
DM*	1/2	$\infty$	0.880	9.8 GB	20 s
<b>Kitti dataset</b>					
SIFT-NN			0.489	0.2 GB	1.7 s
HOG-NN			0.537	2.9 GB	24 s
KPM			0.536	0.3 GB	17 s
GPM			0.661	0.1 GB	2.7 min
DM	1/4	$\infty$	0.800	0.5 GB	2.8 s
DM	1/2	1024	0.812	2.2 GB	5.3 s
DM	1/2	$\infty$	<b>0.856</b>	7.2 GB	14 s
DM*	1/2	$\infty$	0.841	9.9 GB	18 s

**Table 2** Summary of matching performance, run-time and memory usage for the state of the art and DeepMatching (DM). DM\* denotes the preliminary version of DeepMatching published in Weinzaepfel et al (2013). For the proposed method,  $R$  and  $D$  denote the input image resolution and the dictionary size ( $\infty$  stands for no compression). Run-times are computed on 1 core @ 3.6 GHz.

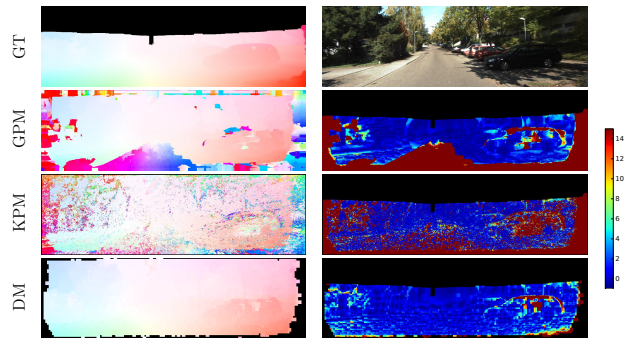


**Fig. 16** Example of matching results on Kitti (pixel displacements have been inferred from matching patches). Left: ground-truth (top) and predicted motion maps for GPM, KPM and DM. To improve visualization, we densified the sparse Kitti ground-truth using bilateral filtering. Right: corresponding error maps. KPM and GPM are not robust to repetitive textures *e.g.* on the road or on trees.

### 5.3 Optical Flow Experiments

We now present experimental results for the optical flow estimation. Optical flow is predicted using the variational framework presented in Section 4.3 that takes as input a set of matches between the two images. In the following, we evaluate the impact of DeepMatching compared to using other matching methods, and compare to the state of the art.



Method	R	D	MPI-Sintel	Kitti	Middlebury
No Match			5.863	8.791	0.274
SIFT-NN			5.733	7.753	0.280
HOG-NN			5.458	8.071	<b>0.273</b>
KPM			5.560	15.289	0.275
GPM			5.561	17.491	0.286
DM	1/2	1024	4.350	7.899	0.320
DM	1/2	$\infty$	<b>4.098</b>	<b>4.407</b>	0.328

**Table 3** Comparison of average endpoint error on different datasets when changing the input matches in the flow computation.

### 5.3.1 Optimization of the parameters

We first optimize the different flow parameters ( $\beta$ ,  $\gamma$ ,  $\delta$ ,  $\sigma$  and  $b$ ) on the MPI-Sintel “small” training set. We employ a gradient descent strategy with multiple initializations followed by a local grid search. For the data term, we find an optimum at  $\delta = 0$ , which is equivalent to removing the color constancy assumption. This can be explained by the fact that the “final” version contains atmospheric effects, reflections, blurs, etc. The remaining parameters are optimal at  $\beta = 300$ ,  $\gamma = 0.8$ ,  $\sigma = 0.5$ ,  $b = 0.6$ .

### 5.3.2 Impact of the matches on the flow

We examine the impact on the flow of different match methods (*i.e.* to be plugged in DeepFlow, see Section 4.3). For each of the matching approaches evaluated above, we use their output as matching term in eq. (18) and optimize the flow parameters on the small training set of MPI-Sintel.

Table 3 shows the endpoint error, averaged over all pixels. Clearly, a sufficiently dense and accurate matching like DM allows to considerably improve the flow estimation on datasets with large displacements (MPI-Sintel, Kitti). Conversely, none of methods above have a tangible effect on the Middlebury dataset, where the displacements are small.

The relatively small gains achieved by SIFT-NN and HOG-NN on MPI-Sintel and Kitti are due to the fact that a lot of regions with large displacements remain uncovered by any matches, such as the sky or the blurred character in the first and second column of Figure 17. Hence, SIFT-NN and HOG-NN have only a limited impact on the variational approach. On the other hand, the gains are also small (or even negative) when using GPM or KPM, despite the fact that they both output dense correspondence fields. We observe for these methods that the weight  $\beta$  of the matching term tends to be small after optimizing the parameters, thus indicating that the matches are found unreliable and noisy during training. The cause is clearly visible in Figure 16,

where large portions containing repetitive textures (*e.g.* road, trees) are incorrectly matched. The poor quality of these matches even leads to a significant drop in performance on the Kitti dataset.

In contrast, DeepMatching obtains dense and accurate matches that enable to boost the optical flow accuracy in case of large displacements. Namely, we observe a relative improvement of 30% on MPI-Sintel and of 50% on Kitti. When using the approximation with 1024 prototypes, however, a significant drop is observed on the Kitti dataset, while the performance remains good on MPI-Sintel. This indicates that approximating DeepMatching can result in a significant loss of robustness when matching repetitive textures, that are more frequent in Kitti than in MPI-Sintel.

### 5.3.3 Results on MPI-Sintel

Table 4 compares our method to state-of-the-art algorithms on the MPI-Sintel test set; parameters are optimized on the “small” training set. A comparison with the preliminary version of DeepFlow (Weinzaepfel et al 2013), referred to as DeepFlow\*, is also provided. In this early version, we used a constant smoothness weight instead of a local one here (see Section 4.3) and used DM\* as input matches. We can see that DeepFlow is among the best performing methods on MPI-Sintel, particularly for large displacements. This is due to the use of a reliable matching term in the variational approach, and this property is shared by all top performing approaches (*e.g.* Revaud et al (2015), Leordeanu et al (2013)). Furthermore, it is interesting to note that among the top performers on MPI-Sintel, 3 methods out of 4 actually employ DeepMatching. In particular, the current best method EpicFlow (Revaud et al 2015) relies on the output of DeepMatching to produce a piece-wise affine flow, and SparseFlowFused (Timofte and Van Gool 2015) combines matches obtained with DeepMatching and an other algorithm. The only method which does not take advantage of DeepMatching is TF+OFM (Kennedy and Taylor 2015), but this approach uses several frames to predict the flow, which other methods do not.

We refer to the webpage of the MPI-Sintel dataset for complete results including the “clean” version.

*Timings.* As mentioned before, DeepMatching at half the resolution takes 15 seconds to compute. The variational part requires 10 additional seconds. DeepFlow consequently takes 25 seconds in total on a single CPU core @ 3.6 GHz. This is in the same order of magnitude as the fastest competitor, EpicFlow (Revaud et al 2015).

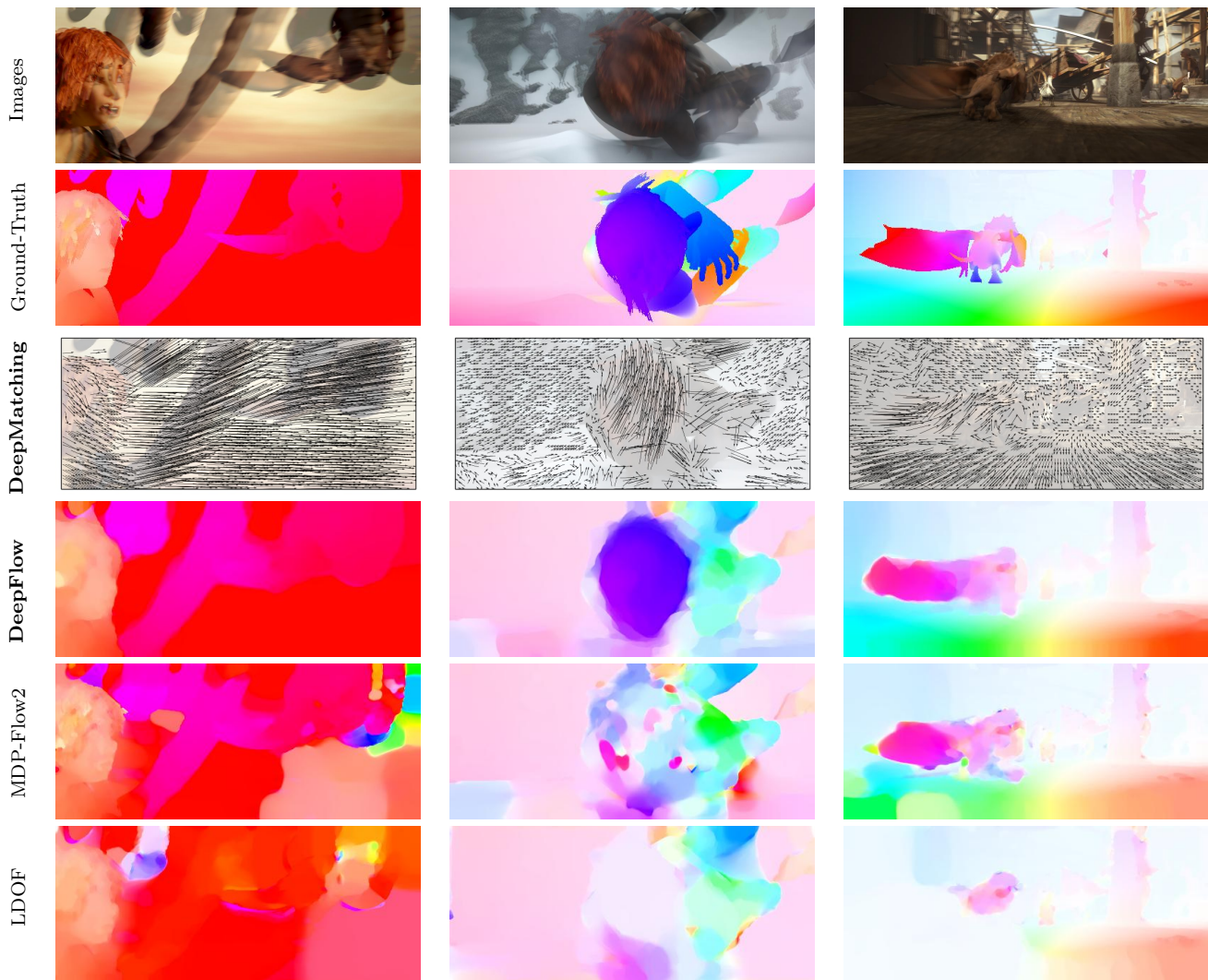


**Fig. 17** Each column shows from top to bottom: two consecutive images, the ground-truth optical flow, our results (*DeepFlow*), and two state-of-the-art methods, LDOF (Brox and Malik 2011) and MDP-Flow2 (Xu et al 2012).

Method	AEE	AEE-occ	s0-10	s10-40	s40+	Time
EpicFlow (Revaud et al 2015)	6.285	32.564	1.135	3.727	38.021	16.4s
TF+OFM (Kennedy and Taylor 2015)	6.727	33.929	1.512	3.765	39.761	~400s
<b>DeepFlow</b>	6.928	38.166	1.182	3.859	42.854	25s
SparsFlowFused Timofte and Van Gool (2015)	7.189	3.286	1.275	3.963	44.319	20
DeepFlow* (Weinzaepfel et al 2013)	7.212	38.781	1.284	4.107	44.118	19s
S2D-Matching (Lecordaux et al 2013)	7.872	40.093	1.172	4.695	48.782	~2000s
LocalLayering (Sun et al 2014a)	8.043	40.879	1.186	4.990	49.426	
Classic+NL-P (Sun et al 2014b)	8.291	40.925	1.208	5.090	51.162	~800s
MDP-Flow2 (Xu et al 2012)	8.445	43.430	1.420	5.449	50.507	709s
NLTGV-SC (Ranftl et al 2014)	8.746	42.242	1.587	4.780	53.860	
LDOF (Brox and Malik 2011)	9.116	42.344	1.485	4.839	57.296	30s

**Table 4** Results on MPI-Sintel test set (final version). AEE-occ is the AEE on occluded areas. s0-10 is the AEE for pixels with motions between 0 and 10 px and similarly for s10-40 and s40+. DeepFlow\* denotes the preliminary version of DeepFlow published in Weinzaepfel et al (2013).

### 5.3.4 Results on Kitti

Table 5 summarizes the main results on the Kitti benchmark (see official website for complete results), when optimizing the parameters on the Kitti training set. AEE-Noc is the AEE computed only in non-occluded

areas. “Out 3” corresponds to the proportion of incorrect pixel correspondences for an error threshold of 3 pixels, *i.e.* it corresponds to  $1 - \text{accuracy}@3$ , and likewise for “Out-Noc 3” for non-occluded areas. In terms of AEE-noc, DeepFlow outperforms the other approaches, but performs somewhat worse in the occluded areas. This is due to a specificity of the Kitti dataset, in which motion is mostly homographic (especially on the image borders, where most surfaces like roads and walls are planar). In such cases, flow is better predicted using an affine motion prior, which locally well approximates homographies (a constant motion prior is used in DeepFlow). As a matter of facts, all top performing methods in terms of total AEE output piece-wise affine optical flow, either due to affine regularizers (BTF-ILLUM (Demetz et al 2014), NLTGB-SC (Ranftl et al 2014),

Method	AEE-noc	AEE	Out-Noc 3	Out 3	Time
<b>DeepFlow</b>	<b>1.4</b>	5.3	6.61%	17.35%	22s
BTF-ILLUM (Demetz et al 2014)	1.5	2.8	6.52%	11.03%	80s
EpicFlow (Revaud et al 2015)	1.5	3.8	7.88%	17.08%	16s
TGV2ADCSIFT (Braux-Zin et al 2013)	1.5	4.5	6.20%	15.15%	12s*
DeepFlow* (Weinzaepfel et al 2013)	1.5	5.8	7.22%	17.79%	17s
NLTGV-SC (Ranftl et al 2014)	1.6	3.8	5.93%	11.96%	16s*
Data-Flow (Vogel et al 2013b)	1.9	5.5	7.11%	14.57%	180s
TF+OFM (Kennedy and Taylor 2015)	2.0	5.0	10.22%	18.46%	350s

**Table 5** Results on Kitti test set. AEE-noc is the AEE over non-occluded areas. Out-Noc 3 (resp. Out 3) refers to the percentage of pixels where flow estimation has an error above 3 pixels in non-occluded areas (resp. all pixels). DeepFlow\* denotes the preliminary version of DeepFlow published in Weinzaepfel et al (2013). • denotes the usage of a GPU.

TGV2ADCSIFT (Braux-Zin et al 2013)) or due to local affine estimators (EpicFlow (Revaud et al 2015)).

Note that the learned parameters on Kitti and MPI-Sintel are close. In particular, running the experiments with the same parameters as MPI-Sintel decreases AEE-Noc by only 0.1 pixels on the training set. This shows that our method does not suffer from overfitting.

### 5.3.5 Results on Middlebury

We optimize the parameters on the Middlebury training set by minimizing the average angular error with the same strategy as for MPI-Sintel. We find weights quasi-zero for the matching term due to the absence of large displacements. DeepFlow obtained an average endpoint error of 0.4 on the test which is competitive with the state of the art.

## 6 Conclusion

We have introduced a dense matching algorithm, called DeepMatching. The proposed algorithm gracefully handles complex non-rigid object deformations and repetitive textured regions. DeepMatching yields state-of-the-art performance for image matching, on resp. the Mikolajczyk (Mikolajczyk et al 2005), the MPI-Sintel (Butler et al 2012) and the Kitti (Geiger et al 2013) datasets. Integrated in a variational energy minimization approach, the resulting approach for optical flow estimation, called DeepFlow, shows competitive performance on optical flow benchmarks, and obtains state-of-the-art results on the MPI-Sintel dataset (Butler et al 2012).

Future work includes incorporating a weighting of the patches in eq. (8) instead of weighting all patches equally to take into account that different parts of a large patches may belong to different objects. This could improve the performance of DeepMatching for thin objects, such as human limbs.

**Acknowledgements** This work was supported by the European integrated project AXES, the MSR/INRIA joint project,

the LabEx PERSYVAL-Lab (ANR-11-LABX-0025), and the ERC advanced grant ALLEGRO.

## References

- Baker S, Scharstein D, Lewis JP, Roth S, Black MJ, Szeliski R (2011) A database and evaluation methodology for optical flow. *IJCV* **2.2**, 5.1
- Barnes C, Shechtman E, Goldman DB, Finkelstein A (2010) The generalized PatchMatch correspondence algorithm. In: *ECCV* **1**, 2.1, 2.2, 5.2.3
- Bengio Y (2009) Learning deep architectures for AI. *Foundations and Trends in Machine Learning* **3.2**
- Black MJ, Anandan P (1996) The robust estimation of multiple motions: parametric and piecewise-smooth flow fields. *Computer Vision and Image Understanding* **2.2**
- Braux-Zin J, Dupont R, Bartoli A (2013) A general dense image matching framework combining direct and feature-based costs. In: *ICCV* **5.3.4**
- Brox T, Malik J (2011) Large displacement optical flow: descriptor matching in variational motion estimation. *IEEE Trans PAMI* **1**, 2.2, 4.3, 5.2.3, 17, 5.3.3
- Brox T, Bruhn A, Papenberger N, Weickert J (2004) High accuracy optical flow estimation based on a theory for warping. In: *ECCV* **2.2**, 4.3
- Bruhn A, Weickert J, Feddern C, Kohlberger T, Schnörr C (2005) Variational optical flow computation in real time. *IEEE Trans on Image Processing* **2.2**, 4.3
- Butler DJ, Wulff J, Stanley GB, Black MJ (2012) A naturalistic open source movie for optical flow evaluation. In: *ECCV (document)*, **1**, 5.1, 6
- Chen Z, Jin H, Lin Z, Cohen S, Wu Y (2013) Large displacement optical flow from nearest neighbor fields. In: *CVPR* **1**
- Dalal N, Triggs B (2005) Histograms of oriented gradients for human detection. In: *CVPR* **1**
- Demetz O, Stoll M, Volz S, Weickert J, Bruhn A (2014) Learning brightness transfer functions for the joint recovery of illumination changes and optical flow. In: *ECCV* **5.3.4**
- Ecker A, Ullman S (2009) A hierarchical non-parametric method for capturing non-rigid deformations. *Image and Vision Computing* **2.1**
- Forsyth D, Ponce J (2011) *Computer Vision: A Modern Approach*. Pearson Education, Limited **1**
- Furukawa Y, Curless B, Seitz SM, Szeliski R (2010) Towards internet-scale multi-view stereo. In: *CVPR* **2.1**
- Geiger A, Lenz P, Stiller C, Urtasun R (2013) Vision meets robotics: The KITTI dataset. *IJRR (document)*, **5.1**, 6
- HaCohen Y, Shechtman E, Goldman DB, Lischinski D (2011) Non-rigid dense correspondence with applications for image enhancement. *SIGGRAPH* **1**, 2.1, 4.2, 5.1, 5.2.3
- Horn BKP, Schunck BG (1981) Determining Optical Flow. *Artificial Intelligence* **2.2**
- Kennedy R, Taylor CJ (2015) Optical flow with geometric occlusion estimation and fusion of multiple frames. In: *EMM-CVPR* **5.3.3**, 5.3.4
- Keysers D, Deselaers T, Gollan C, Ney H (2007) Deformation models for image recognition. *IEEE Trans PAMI* **2.1**
- Kim J, Liu C, Sha F, Grauman K (2013) Deformable spatial pyramid matching for fast dense correspondences. In: *CVPR* **2.1**
- Korman S, Avidan S (2011) Coherency sensitive hashing. In: *ICCV* **2.1**
- LeCun Y, Bottou L, Bengio Y, Haffner P (1998a) Gradient-based learning applied to document recognition. *Proceedings of the IEEE* **2.1**, 3.2, 3.4

- LeCun Y, Bottou L, Orr G, Muller K (1998b) Efficient backprop. In: *Neural Networks: Tricks of the trade* 3.2
- Leordeanu M, Zanfir A, Sminchisescu C (2013) Locally affine sparse-to-dense matching for motion and occlusion estimation. In: *ICCV* 2.2, 5.3.3
- Liu C, Yuen J, Torralba A (2011) SIFT flow: Dense correspondence across scenes and its applications. *IEEE Trans PAMI* 2.2
- Lowe DG (2004) Distinctive image features from scale-invariant keypoints. *IJCV* 1, 2.2, 3.1, 4.2, 5.2.3
- Malik J, Perona P (1990) Preattentive texture discrimination with early vision mechanisms. *Journal of the Optical Society of America A: Optics, Image Science, and Vision* 3.2
- Mikolajczyk K, Tuytelaars T, Schmid C, Zisserman A, Matas J, Schaffalitzky F, Kadir T, Gool LV (2005) A comparison of affine region detectors. *IJCV* (document), 2.1, 4.2, 5.1, 6
- Muja M, Lowe DG (2009) Fast approximate nearest neighbors with automatic algorithm configuration. In: *International Conference on Computer Vision Theory and Application VISSAPP'09*, INSTICC Press 5.2.3
- Papenberg N, Bruhn A, Brox T, Didas S, Weickert J (2006) Highly accurate optic flow computation with theoretically justified warping. *IJCV* 2.2
- Philbin J, Isard M, Sivic J, Zisserman A (2010) Descriptor learning for efficient retrieval. In: *ECCV* 2.1
- Ranftl R, Bredies K, Pock T (2014) Non-local total generalized variation for optical flow estimation. In: *ECCV* 5.3.3, 5.3.4
- Revaud J, Weinzaepfel P, Harchaoui Z, Schmid C (2015) EpicFlow: Edge-Preserving Interpolation of Correspondences for Optical Flow. In: *CVPR* 5.3.3, 5.3.3, 5.3.4
- Stoll M, Volz S, Bruhn A (2012) Adaptive integration of feature matches into variational optical flow methods. In: *ACCV* 4.3
- Sun D, Liu C, Pfister H (2014a) Local layering for joint motion estimation and occlusion detection. In: *CVPR* 5.3.3
- Sun D, Roth S, Black M (2014b) A quantitative analysis of current practices in optical flow estimation and the principles behind them. *IJCV* 2.2, 4.3, 5.3.3
- Sun J (2012) Computing nearest-neighbor fields via propagation-assisted kd-trees. In: *CVPR* 2.1, 5.2.3
- Szeliski R (2010) *Computer Vision: Algorithms and Applications*. Springer 1, 2.1, 4.2
- Timoftre R, Van Gool L (2015) Sparse flow: Sparse matching for small to large displacement optical flow. In: *Applications of Computer Vision (WACV)* 5.3.3
- Tola E, Lepetit V, Fua P (2008) A fast local descriptor for dense matching. In: *CVPR* 2.2
- Uchida S, Sakoe H (1998) A monotonic and continuous two-dimensional warping based on dynamic programming. In: *ICPR* 2.1
- Vogel C, Roth S, Schindler K (2013a) An evaluation of data costs for optical flow. In: *GCPR* 2.2
- Vogel C, Schindler K, Roth S (2013b) Piecewise rigid scene flow. In: *ICCV* 5.3.4
- Wedel A, Cremers D, Pock T, Bischof H (2009) Structure- and motion-adaptive regularization for high accuracy optic flow. In: *ICCV* 4.3
- Weinzaepfel P, Revaud J, Harchaoui Z, Schmid C (2013) Deepflow: Large displacement optical flow with deep matching. In: *ICCV* 1, 3.3, 3.3, 5.2.3, 2, 5.3.3, 4, 5.3.4, 5
- Werlberger M, Trobin W, Pock T, Wedel A, Cremers D, Bischof H (2009) Anisotropic Huber-L1 optical flow. In: *BMVC* 2.2
- Wills J, Agarwal S, Belongie S (2006) A feature-based approach for dense segmentation and estimation of large disparity motion. *IJCV* 2.1
- Xu L, Jia J, Matsushita Y (2012) Motion detail preserving optical flow estimation. *IEEE Trans PAMI* 1, 2.2, 4.3, 17, 5.3.3
- Zimmer H, Bruhn A, Weickert J (2011) Optic flow in harmony. *IJCV* 4.3